Materials Advances

ROYAL SOCIETY OF CHEMISTRY

PAPER

View Article Online
View Journal | View Issue

Check for updates

Cite this: *Mater. Adv.*, 2023, 4, 2192

Green pepper-derived hierarchical porous carbon for supercapacitors with high performance†

Yicheng Zeng,‡[a] Fuming Zhang,‡[a] Jinggao Wu[b] and Jing Huang *[a]

Received 25th January 2023,
Accepted 3rd April 2023

DOI: 10.1039/d3ma00045a

rsc.li/materials-advances

Renewable, low-cost and environmentally friendly porous carbon for high performance carbon electrode materials has attracted considerable attention in the energy conversion and storage fields. Herein, we have developed a sustainable route to fabricate porous carbon materials derived from green peppers through conventional thermal annealing and KOH-activation. The as-prepared GPAC-4 with a hierarchical porous structure exhibits a high specific surface area of 1052.70 $m^2\ g^{-1}$ and a high capacitance of 863.1 F g^{-1} at 1 A g^{-1} as well as a good capacitance retention ratio of 97.80% at 10 A g^{-1} over 10 000 cycles. Moreover, the assembled supercapacitor exhibits a capacitance of 214.45 F g^{-1} at 1 A g^{-1}, which corresponds to a maximum energy of 42.89 W h kg^{-1} at a power density of 1.2 kW kg^{-1}. Furthermore, the supercapacitor demonstrates good cycling stability with a low loss of 3.73% over 10 000 charge–discharge cycles. These findings could open up an exciting field for exploring reproducible vegetables as the raw materials for high performance supercapacitors.

1. Introduction

With the aggravating environmental pollution and energy crisis in recent years, it is urgent to exploit renewable and clean energy sources (*e.g.*, solar and wind power) and to develop cost-effective, environmentally friendly and high performance electrochemical energy storage technology/devices.[1–3] However, traditional energy sources are no longer able to meet the requirements for human production and life in the developed economic society.[4,5] Among different types of energy storage devices, supercapacitors have received considerable attention owing to their high power density, outstanding cyclability, long life, and short charging time.[6,7] Based on their energy storage mechanisms, supercapacitors usually have been classified as electrical double-layer capacitors (EDLCs) and pseudocapacitors, as well as hybrid capacitors.[8,9] Electric double-layer capacitors store energy through rapid and reversible adsorption of electrolyte ions onto the surface of the electrodes, which are heavily influenced by the specific surface area and porosity of electrode materials.[10,11]

Currently, the electrode active materials of supercapacitors are divided into three types: metal oxides, electronically conducting polymers and carbon materials.[12,13] Among them, carbon materials have been commercially used as supercapacitor electrode materials for several decades such as activated carbons, carbon fibers, carbon nanotubes, carbon aerogels, graphene and carbide derived carbons.[14,15] Porous carbons have attracted particular interest for their special properties, such as large surface area, surface hydrophobicity/hydrophilicity, large pore volume, chemical inertness, good mechanical and thermal stabilities, ease of handling, and low-cost preparation.[16,17]

However, the applications of conventional carbon materials are largely restricted owing to the high cost of raw materials such as mineral materials and petroleum, environmental destructiveness of preparation procedures, complicated manufacturing and relatively low energy density.[18,19] Accordingly, researchers have made considerable efforts to form favorable porous carbon materials derived from green reproducible biomass or their derivatives, which are critical for sustainable development and environmental protection.[20,21] Moreover, biomass-derived porous carbon materials are generally composed of unique micro/nanostructures and heteroatoms originating from biomass precursors, which could contribute to the surface wettability of the carbon materials, rapid electrolyte ion transport within the nanostructure and further improvement of the electrochemical performance.[22,23] Additionally, the application of the carbon derived from biomass renewable materials for supercapacitors could not only provide methods for dealing with the scarcity of fossil fuels, but also take full advantages of renewable natural resources.[24,25]

---

[a] *State Key Laboratory of Silkworm Genome Biology; College of Sericulture, Textile and Biomass Sciences; Westa College, Southwest University, Chongqing 400715, P. R. China. E-mail: hj41012@163.com*

[b] *Key Laboratory of Rare Earth Optoelectronic Materials & Devices, College of Chemistry and Materials Engineering, Huaihua University, Huaihua 418000, P. R. China*

† Electronic supplementary information (ESI) available. See DOI: **https://doi.org/10.1039/d3ma00045a**

‡ Equal contribution to this work.

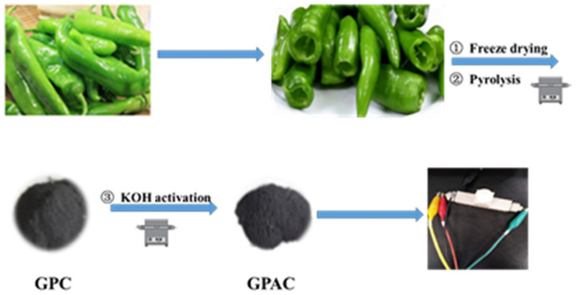

Scheme 1 Synthetic procedure of porous carbon from green peppers.

Green peppers as a kind of vegetable belong to the capsicum plants of the solanaceae family, which is widely distributed in many regions of the world. Green peppers are rich in dietary fibers, capsaicin, and vitamin C. Currently, green peppers are usually used as food in our daily life. Based on the aforementioned discussion, we present a facile and scalable strategy to utilize natural green peppers as biomass precursors to fabricate porous carbon electrode materials through carbonization and chemical activation of KOH, and to develop environmentally benign full supercapacitor devices (Scheme 1). In this context, we have optimized the reaction temperature and alkali concentration and demonstrated the relationship between the structure and the electrochemical performance.

2. Experimental section

2.1. Materials and methods

2.1.1. Materials and reagents. Green peppers were purchased from a local market in Chongqing, China, and the green peppers' skins were collected after removing the green peppers' seeds and dried by freezing. Nafion solution, acetylene black, poly(tetrafluoroethylene) (PTFE), and ethanol were purchased from Sigma-Aldrich. Potassium hydroxide (KOH) and all other reagents were obtained from Adamas-beta®. All chemicals were used without further purification.

2.1.2. Preparation of green pepper-derived activated carbon (GPAC). The peels of green peppers were first washed with distilled water to remove dusts and other inorganic impurities, followed by cutting into pieces and drying by vacuum freeze-drying. The dried peels were then well ground to powders, prior to the carbonization step. The preparation of activated carbon is a two-stage process of carbonization and activation. Firstly, the green peppers were heated in a tubular furnace under an argon atmosphere to 800 °C at a heating rate of 5 °C min^{-1}, and then held the temperature for 2 hour. The obtained carbon was named GPC. In the second step, GPC and KOH with a mass ratio of 1 : 1.5 were thoroughly ground using an agate mortar. After grinding, the power was further heated at 800 °C for 2 hours under the same heating conditions. Finally, the obtained carbon was named GPAC-4. For comparison, the different mass ratios of GPC/KOH (2 : 1, 1.5 : 1, 1 : 1, and 1 : 2) were also investigated using the above process. The samples were denoted as GPAC-1, GPAC-2, GPAC-3 and GPAC-5. In addition, GPAC-6, GPAC-7 and GPAC-8 were prepared at 600, 700 and 900 °C in accordance with a similar procedure to that for GPAC-4. In the whole process, all carbonized samples were drastically washed with diluted HCl and deionized water, and then dried at 80 °C for 12 h.

2.2. Characterization

The XRD patterns of all samples were recorded using powder X-ray diffraction (Shimadzu XRD-7000). The surface morphology and structure of samples were observed using scanning electron microscopy (FESEM, JSM-7800F) and transmission electron microscopy (TEM, JEOL 2100). Nitrogen sorption isotherms were obtained using an Autosorb-1 analyzer (Quantachrome Instruments). The specific surface area was calculated using the modified Brunauer–Emmett–Teller (BET) method. The pore size distributions and the pore volume were analyzed from the adsorption branch isotherms using a density functional theory (DFT) method. Moreover, the total pore volume (V_t) was estimated from the amount adsorbed at a relative pressure P/P_0 of 0.990. The micropore volume (V_{mic}) and micropore surface area (S_{mic}) were determined by the t-plot theory. Raman spectra were acquired using a Jobin-Yvon HR 800 spectrometer. X-ray photoelectron spectroscopy (XPS) measurements were performed using a Thermo Fisher Scientific Escalab 250xi spectrometer, USA. Fourier transform infrared (FT-IR) spectra were recorded using a Thermo Scientific Nicolet iS 50 spectrometer.

2.3. Electrochemical measurements

For the two-electrode system, a homogeneous slurry of the electroactive material, polytetrafluoroethylene (PTFE), and acetylene black with a weight ratio of 80 : 10 : 10 in ethanol was formed, pasted onto the nickel foam current collector (1 cm × 1 cm), and then vacuum dried at 80 °C for 12 h. The loading of the active material for each working electrode was measured to be $\sim$3 mg cm^{-2}. And then, a glass-fiber filter paper (Waterman, GF/B) as a separator and 1 M KOH aqueous solution as the electrolyte were used to assemble a test cell. For the three-electrode system, the working electrode was manufactured *via* the dispersion of active carbon in the mixture of Nafion and ethanol (1 : 20) dropping on the glassy carbon electrode, accompanying with platinum foil Hg/HgO as the counter and reference electrodes, respectively. Electrochemical characterization was carried out using an electrochemical workstation (Shanghai Chenhua Instrument Co. Ltd, China).

For the two-electrode system, the gravimetric specific capacitance of a single electrode is calculated using the following equation:

$$C_{\mathrm{sp}} = 2I \times \Delta t/m \times \Delta V \tag{1}$$

where C_{sp} (F g^{-1}) is the specific capacitance based on the mass of the active carbons, where I is the discharge current (A), Δt is the discharge time (s), ΔV is the voltage difference (except the ohm drop) within Δt (V), and m is the loading of the active material in each working electrode (g).

For the three-electrode system, the gravimetric specific capacitance can be calculated using the following equations:

$$C_{sp} = I \times \Delta t/m \times \Delta V \quad (2)$$

where I is the discharge current (A), Δt is the discharge time (s), ΔV is the voltage (V), and m is the mass of the active materials (g).

The energy density E (W h kg^{-1}) and the power density P (W kg^{-1}) are calculated using the following equations:

$$E = C_{sp}V^2/(2 \times 3.6) \quad (3)$$

$$P = 3600E/\Delta t \quad (4)$$

where t is the discharge time (s).

3. Results and discussion

3.1. Material characterization

The SEM image of GPAC-4 (Fig. 1a) indicates a rough surface with interconnected quasi-spherical carbon particles and a uniformly distributed honeycomb pore structure on the rough carbon surface. The transmission electron microscopy (TEM) image of GPAC-4 (Fig. 1b) manifests a distinct carbon skeleton and a multilayer distribution of nanopore structures with a hierarchical pore arrangement and thin pore walls, which contributes to the electrochemical performance and the electrical conductivity of the carbon material.[26]

The XRD patterns of GPAC-4 and GPC (Fig. 1c) indicate two characteristic peaks located at 2θ values of $\sim 22^\circ$ and $\sim 43^\circ$, which correspond to the (002) and (100) diffraction peaks in the graphite structure of carbon planes.[27] Moreover, the broad intensity of the (002) peak also confirms an amorphous carbon structure.[28] And then, the degree of disorder within the carbon material is also explored using Raman spectroscopy (Fig. 1d). The two characteristic peaks at 1350 cm^{-1} and 1590 cm^{-1} correspond to the characteristic peaks in the D-band and G-band of samples, respectively.[29] The D-band is attributed to the disordered structures of carbon and the G-band is related to graphite in-plane vibrations. Therefore, I_D represents the degree of carbon disorder, while I_G stands for the sp^2 graphitised structure of carbon.[30] The I_D/I_G ratios of GPC and GPAC-4 (1.046 and 1.017, respectively) reveal the enhancement of graphitization after KOH activation.

FT-IR spectra at wavelengths of 400–4000 cm^{-1} could reveal the functional groups and structural transformations on the surface of the sample. As described in Fig. S1 (ESI†), the wider absorption peak centered at 3438 cm^{-1} is attributed to –NH in the amide group. The absorption peaks at 2927 cm^{-1} and 2852 cm^{-1} are attributed to the stretching vibration of aliphatic $-CH_2$. The band at 1608 cm^{-1} is ascribed to $-C{=}O$. Absorption peaks are indicated at around 1100 cm^{-1} due to –C–O vibrations.[31] Infrared investigations demonstrate the presence of carbon-containing groups in the carbon materials, which contributes to the hydrophilicity and chemical stability of the material in electrolyte solutions.[32]

To evaluate the chemical identities of the heteroatoms in the functionalized GPAC-4, XPS measurements are carried out. The X-ray photoelectron spectroscopy (XPS) survey spectrum of GPAC-4 (Fig. S2, ESI†) confirms the presence of C, O, N, P and S, which could lead to pseudocapacitance and further contribute to the whole capacitance during the charge/discharge process. The high-resolution C1s spectrum of GPAC-4 (Fig. 1f) could be deconvoluted into five individual component peaks, which corresponds to C=C (284.8 eV), S-sp^3C (285 eV), C–O/C–O–C (286.3 eV), C=O (288.6 eV) and π–π^* (289.1 eV).[33] The spectrum of N 1s (Fig. 1g) could be convolved into five binding energies at 398.5, 399.5, 400.4, 401.7 and 404.4 eV corresponding to pyridinic-N, quaternary-N, amides/amines or nitrile N, pyrrolic-N and N-oxides, respectively.[34] The XPS spectrum of O1s (Fig. 1h) could be convolved into two groups of peaks, such as P=O (531.7 eV) and P–O–P/P–O–C (533.2 eV). The oxygen-containing functional groups could increase the surface wettability of carbon materials.[35] The XPS spectrum of P2p, with three peaks at 131.8, 133.4 and 134.4 eV, corresponds to three types of chemical bonds, namely, C-P species, pyrophosphate/polyphosphate (PP) and monophosphate/metaphosphate (MP). The presence of P could effectively result in the increase of the carbon layer spacing, and further facilitate the diffusion of electrolyte ions to the interior of the electrode. The doping of P atoms could also introduce specific defects that refrain from the formation of unstable carboxyl groups and further improve the electrochemical stability of the electrode material.[36] The convolution peaks in the S2p region of S elements could be divided into three peaks which correspond to the C=S (161.8 eV), C–S (164.5 eV) and oxides of S (167.5 eV), respectively.[37] In general, the introduction of heteroatoms into the carbon skeleton could change the original structure of the material surface and further lead to the carbon surface more disordered, which may generate the pseudocapacitance and further improve the electrical conductivity and wettability of the carbon materials.[38]

The isotherms of GPAC-4 indicate the characteristics of the type IV isotherm with a H_4 hysteresis loop (Fig. 1e). For isotherms, the curve rapidly increases at lower relative pressures ($P/P_0 < 0.1$) due to the presence of micropores, which demonstrates the sufficient storage space for electrolyte ions.[39] And then, the presence of a significant hysteresis loop at 0.4–0.8 P/P_0 is ascribed to the large number of mesoporous structures.[40] As the pressure goes on increasing, a significant increase of the adsorption at high relative pressures ($P/P_0 > 0.9$) represents the small number of macropores in the carbon.[41] Compared with this, GPC exhibits the typical type V adsorption–desorption isotherm with a H_4 hysteresis loop. In more detail, the characteristics of the obtained various ACs are listed in Table 1. GPAC-4 manifests a Brunauer–Emmett–Teller (BET) specific surface area of 1052.70 $m^2\ g^{-1}$ and a pore volume (0.9898 $cm^3\ g^{-1}$) much higher than that of GPC (245.49 $m^2\ g^{-1}$ and 0.984 $cm^3\ g^{-1}$). The phenomenon is ascribed to the etching and intercalation effects of KOH, which could regulate the synthesis of porous carbon materials.[42] During the pyrolysis process, the release of decomposition

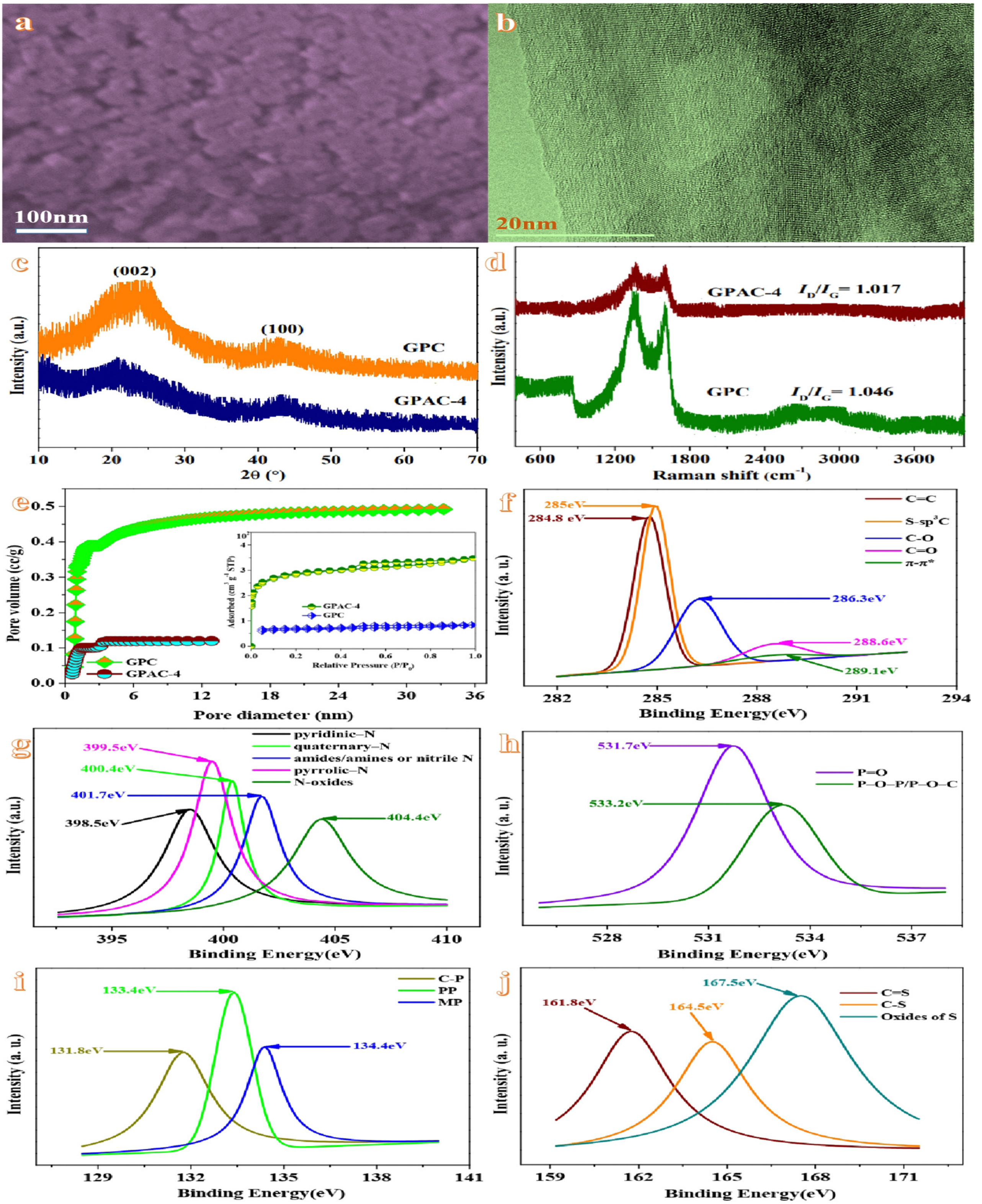

Fig. 1 (a) FESEM image of GPAC-4. (b) TEM image of GPAC-4. (c) XRD patterns of GPC and GPAC-4. (d) Raman spectra of GPC and GPAC-4. (e) N_2 adsorption/desorption isotherms (inset photograph) and the pore size distributions of GPC and GPAC-4. (f) High resolution C1s of GPAC-4. (g) High resolution N1s of GPAC-4. (h) High resolution O2p of GPAC-4. (i) High resolution P2p of GPAC-4. (j) high resolution S2p of GPAC-4.

Table 1 Summary of the BET characteristics of activated carbons

Sample	S_{BET}[a]	V_{tot}[b]	S_{mi}[c]	S_{me}[d]	S_{ma}[e]	V_{mi}[f]	V_{me}[g]	V_{ma}[h]
GPC	245.49	0.984	102.47	96,35	46.66	0.37	0.42	0.194
GPAC-1	784.62	0.532	263.47	386.52	134.63	0.15	0.32	0.062
GPAC-2	975.34	0.627	153.27	572.84	249.23	0.105	0.426	0.096
GPAC-3	854.67	0.751	213.75	483.26	157.66	0.106	0.525	0.12
GPAC-4	1052.7	0.9898	157.84	753.62	141.24	0.142	0.568	0.28
GPAC-5	987.65	0.864	115.62	634.71	237.32	0.158	0.613	0.093
GPAC-6	573.58	0.851	91.63	387.42	94.53	0.136	0.638	0.077
GPAC-7	654.21	0.724	105.36	473.82	75.03	0.103	0.517	0.104
GPAC-8	752.46	0.687	113.57	513.72	125.17	0.126	0.483	0.078

[a] SBET: BET surface area. [b] V_{tot}: total volume. [c] S_{mi}: micropore surface area. [d] S_{me}: mesopore surface area. [e] S_{ma}: macropore surface area. [f] V_{mi}: micropore volume. [g] V_{me}: mesopore volume. [h] V_{ma}: macropore volume.

products, such as H_2O, CO, CO_2, and NH_3, will open up closed pores, and further result in the formation of meso-/macropores.[43] Meanwhile, the alkali metal K is intercalated into the carbon lattice, which leads to the formation of large pores. And then, the pore volume is further increased, accompanying with the removal of the metal residue through hydrochloric acid washing.[44] Apart from this, different temperatures also impart an effect on the textural parameters of carbon materials. With the temperature increasing from 600 to 800 °C, both surface areas (from 573.58 to 654.21 to 1052.70 $m^2\ g^{-1}$) and volumes (from 0.851 to 0.724 to 0.9898 $cm^3\ g^{-1}$) increase in the same way. Although the temperature varying from 600 to 800 °C could lead to the increase of micro-mesopores' specific surface area and pore volume, the macropores do not indicate a similar phenomenon. When the temperature goes on further increasing to 900 °C, the pores may collapse, which unfavorably result in the decrease of the textural properties (752.46 $m^2\ g^{-1}$ and 0.687 $cm^3\ g^{-1}$). On account of the pore size distribution curve of GPAC-4, most pores are mesopores ranging from 2 to 15 nm, which could provide transport channels for ions. The average pore sizes of GPAC-4 and GPC are 3.304 nm and 3.137 nm, respectively. The activation of KOH could contribute to the increasing textural properties and further maximizing the ion adsorption sites,[45] owing to the generation of a huge amount of gases (CO and CO_2) during the activation procedure. In addition, this hierarchical pore structure endows GPAC-4 with the properties for high performance supercapacitors. Macropores could accommodate the electrolyte, which could shorten the travel distance of electrolyte ions during the charge and discharge process. Mesopores could afford a wide transport channel for the electrolyte ions to reach the micropores quickly to accomplish the charge storage.[46]

3.2. Electrochemical behaviors of the electrode

To verify the potential application of green pepper-derived porous carbon in electrochemical processes, the active working electrodes fabricated by using the as-prepared GPACs have been investigated. The GPACs' electrodes are evaluated electrochemically using three electrodes assembled in virtue of the electrochemical workstation using a Hg/HgO electrode as a reference electrode and a platinum wire electrode as the counter electrode as well as 1 mol L^{-1} KOH as the electrolyte. As described in Fig. 2a, the CV curves present a slightly deviated rectangular shape without significant deformation at scan rates from 2 to 200 mV s^{-1}, which reveal the dominant electrochemical double layer capacitance, along with the contribution of pseudocapacitance.[47] The curves with a quasi-rectangular shape could still be maintained even at a high rate of 200 mV s^{-1}, which reveals the superior rate capability. The presence of weak peaks in CV curves could be attributed to reversible redox reactions, which demonstrates the synergistic contribution of the bilayer capacitance from carbon and the pseudocapacitance from heteroatom doping and functional groups.[48] Additionally, the CV curve of GPAC-4 exhibits the largest integral area compared with other GPAC samples and GPC (Fig. S3, ESI†) at a scan rate of 100 mV s^{-1}, which confirms the largest specific capacity. Significantly, the construction of the heterostructure is beneficial to monitor the electronic structure and provides more active sites to heighten the transportation of electrons and ions.[49] For the galvanostatic charge/discharge (GCD) curves (Fig. 2b) at a current density from 1 to 20 A g^{-1}, a quasi-triangle shape with a linear voltage–time relationship are maintained, which reflects the capacitive behavior.[50] However, the triangles tend to shift towards the right and further lead to the increase of the final discharge time, which may be ascribed to the pseudocapacitance derived from the heteroatomic groups. Moreover, the synergistic effect of the bilayer properties and pseudocapacitance behaviour can contribute to the electrochemical performance of the electrodes.[51] Based on GCD curves, the specific capacitance of GPAC-4 is as high as 863.1 F g^{-1} at 1 A g^{-1}, which is higher than many other biomass-derived materials[52–57] and also agree well with the CV results. Even at a high current density of 20 A g^{-1}, the specific capacitance of 258.66 F g^{-1} could be still obtained, owing to the ultra-high mesoporous volume providing more favourable channels for electrolyte ions to reach the electrolyte/electrode interface to complete the charge storage.[58] The green pepper-derived GPAC-4 with well-developed hierarchical pores and the heteroatom-doped skeleton is a suitable electrode for supercapacitors.

AC impedance tests are performed to verify the internal ion transport and equivalent resistance characteristics of the electrodes. Nyquist curves (Fig. 2c) indicate a typical form, with a slight arc and a slight curvature in the high-frequency region, and a curve with an angle of approximately 45° in the medium frequency region as well as a nearly vertical straight line in the low-frequency region.[59] The intercept along the Z' axis in the high-frequency region represents the internal resistance generated by the interfacial contact resistance of the material using the current collector, the ohmic resistance of the electrolyte and the intrinsic resistance of the current collector. The diameter of the slight arc of the solid axis in the high frequency region represents the charge transfer resistance generated at the interface between the electrode material and the electrolyte. The Warburg reaction in the medium frequency region represents the impedance generated by ion diffusion in the porous structure of the electrode material. The extremely short medium

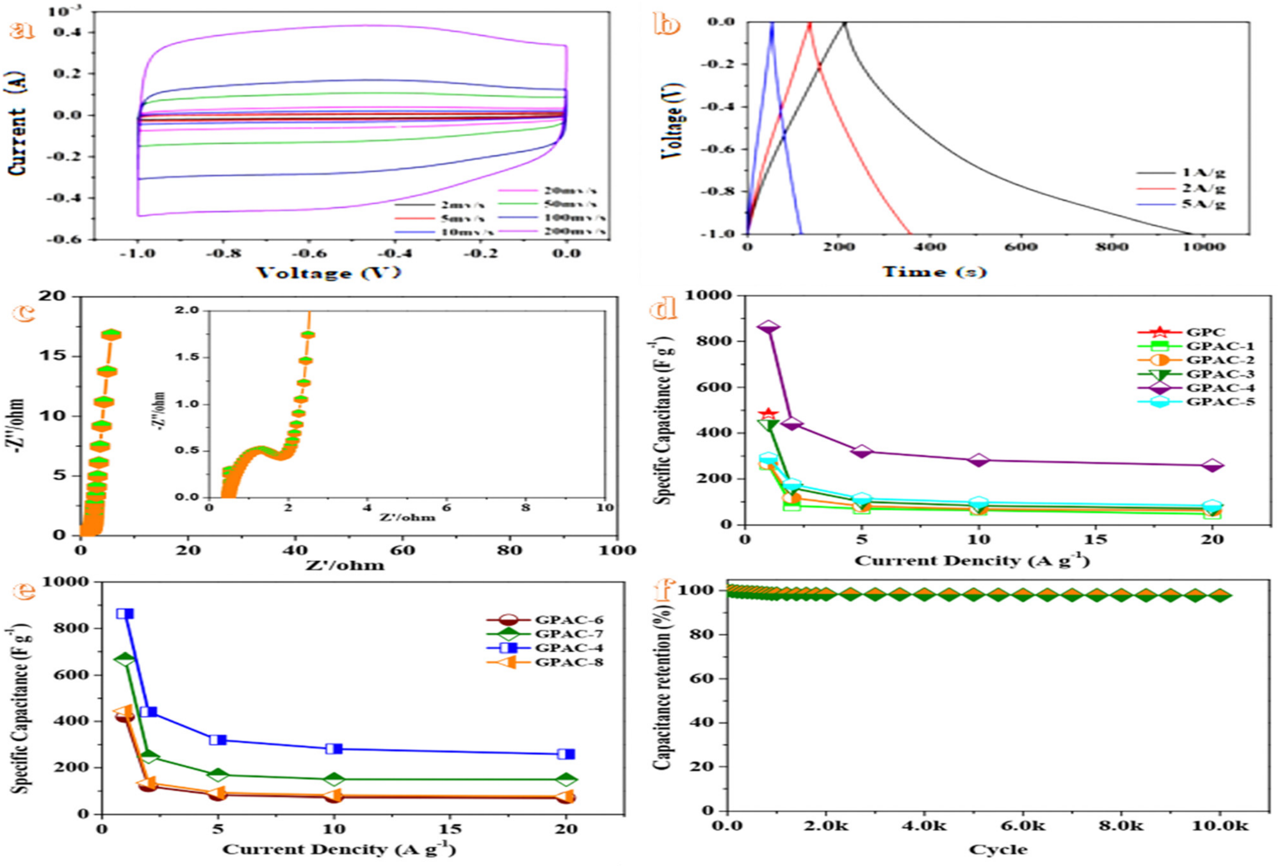

Fig. 2 (a) CV curves of GPAC-4 at different scan rates. (b) Galvanostatic charge/discharge curves of GPAC-4 at different current densities. (c) Nyquist plots of GPAC-4. (d) Capacitances of GPAC samples prepared using different ratios of precursor/KOH at different current densities. (e) Capacitances of GPAC samples prepared at different temperatures at different current densities. (f) Cycling performance of GPAC-4 at 10 A g^{-1}.

frequency region represents the fast ion transfer rate of the internal electrode.[60] Based on the Nyquist curves, the GPAC-4 electrode demonstrates the best ion transfer and charge transfer performance with a low internal resistance value of $\sim$0.4 Ω.

The specific capacitances of GPAC samples at different current densities are presented in Fig. 2d and e. Compared with GPC (483.47 F g^{-1} at 1 A g^{-1}), the specific capacitance increases to 863.1 F g^{-1} at 1 A g^{-1}(GPAC-4), owing to the activation of KOH. Additionally, GPAC-4 offers a much higher specific capacity than other GPACs at all current densities. As for GPAC-4, the specific capacity values are 863.10, 441.46, 319.85, 281.33 and 258.66 F g^{-1} at 1, 2, 5, 10, and 20 A g^{-1}, respectively. Additionally, the capacitance of all the GPAC samples decrease with the increase of the current density, which could be mainly ascribed to the weaker diffusion ability of electrolyte ions at high current densities and further result in the incomplete utilization of the pores of the active electrode material.[61]

Cycling stability is an important parameter of the GPAC-4 electrode in practical applications. Surprisingly, the GPAC-4 electrode maintains 97.80% retention of the initial specific capacity at 10 A g^{-1} over 10 000 cycles in Fig. 2f, which demonstrates an excellent cycling stability. The superior cyclability could be attributed to the increase of conductivity and the reaction kinetics along with the cycling process, owing to the heterostructure and abundant defects (Fig. 3).[62] The excellent electrochemical reusability makes the GPAC-4 electrode a perfect match for the construction of the supercapacitor.

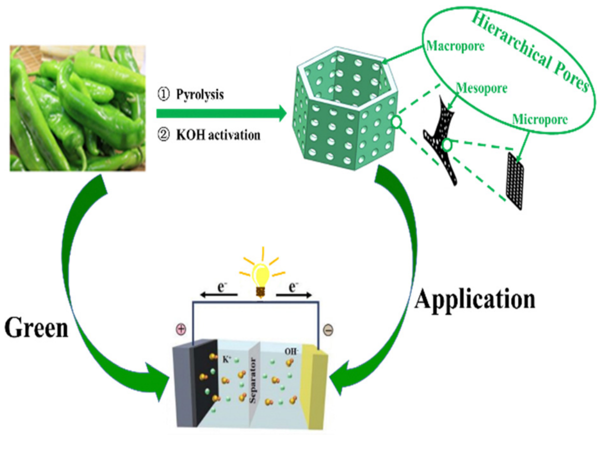

Fig. 3 Schematic diagram of the formation of the supercapacitor.

3.3. Electrochemical behavior of the supercapacitor

To further investigate the practical performance of GPAC-4, a symmetric supercapacitor (GPAC-4//GPAC-4) is constructed in

1 M KOH as the alkaline electrolyte to conduct a two-electrode electrochemical performance evaluation. As described in Fig. 4a, the CV curves with the gradually increasing scan rate from 2 to 200 mV s^{-1} in the voltage ranging from 0 to 1.2 V indicate a symmetrical rectangular shape without significant shape distortions, which highlights the rapid ionic transport process and reversible electrochemical reactions.[63]

GCD curves of the assembled supercapacitor exhibit an approximate isosceles triangle (Fig. 4b), which reveals the good capacitance characteristics and good coulombic efficiency.[64] Defective microporous carbon materials could increase the faradaic/non-faradaic reaction sites on the surface/near-surface region and simultaneously constrain the ion diffusion path, and further improve the conductive pathways.[65] On account of GCD curves at different current densities (Fig. 4c), the excellent specific capacitance of 214.45 F g^{-1} at a current density of 1 A g^{-1} is obtained. Even when the current density increases by 20 times to 20 A g^{-1}, a high capacitance of 177.67 F g^{-1} with a rate retention of 82.85% could still be maintained, which demonstrates the excellent rate performance of the supercapacitor. Simultaneously, the corresponding areal specific capacitances of 0.429F cm^{-2} at 1A g^{-1} and 0.355 F g^{-1} at 20 A g^{-1} are also deduced. Additionally, the capacitance retention decreases from 214.45 F g^{-1} to 177.67 F g^{-1} accompanying with the current density ranging from 1 to 20 A g^{-1}. At low current densities, ions move slowly during charging, which leads to a large amount of charges accumulating on the porous surface and higher specific capacitance. Meanwhile, at high current densities, ions move faster, which results in a short time for charge accumulation on the porous surface, and further lower specific capacitance.[66]

Electrochemical impedance spectroscopy (EIS) measurements are carried out in the frequency range of 0.01 Hz to 100 kHz. The Nyquist curve of the supercapacitor (Fig. 4d) exhibits a semicircle in the high-frequency region and a sloping line in the low-frequency region, which could be attributed to the charge-transfer resistance and the Warburg impedance, respectively.[67] The semicircle on the EIS plot indicates a small charge transfer resistance, which confirms good charge transfer kinetics.[68] The low internal resistance value of ~0.5 Ω could be ascribed to the introduction of heteroatom-doping and the

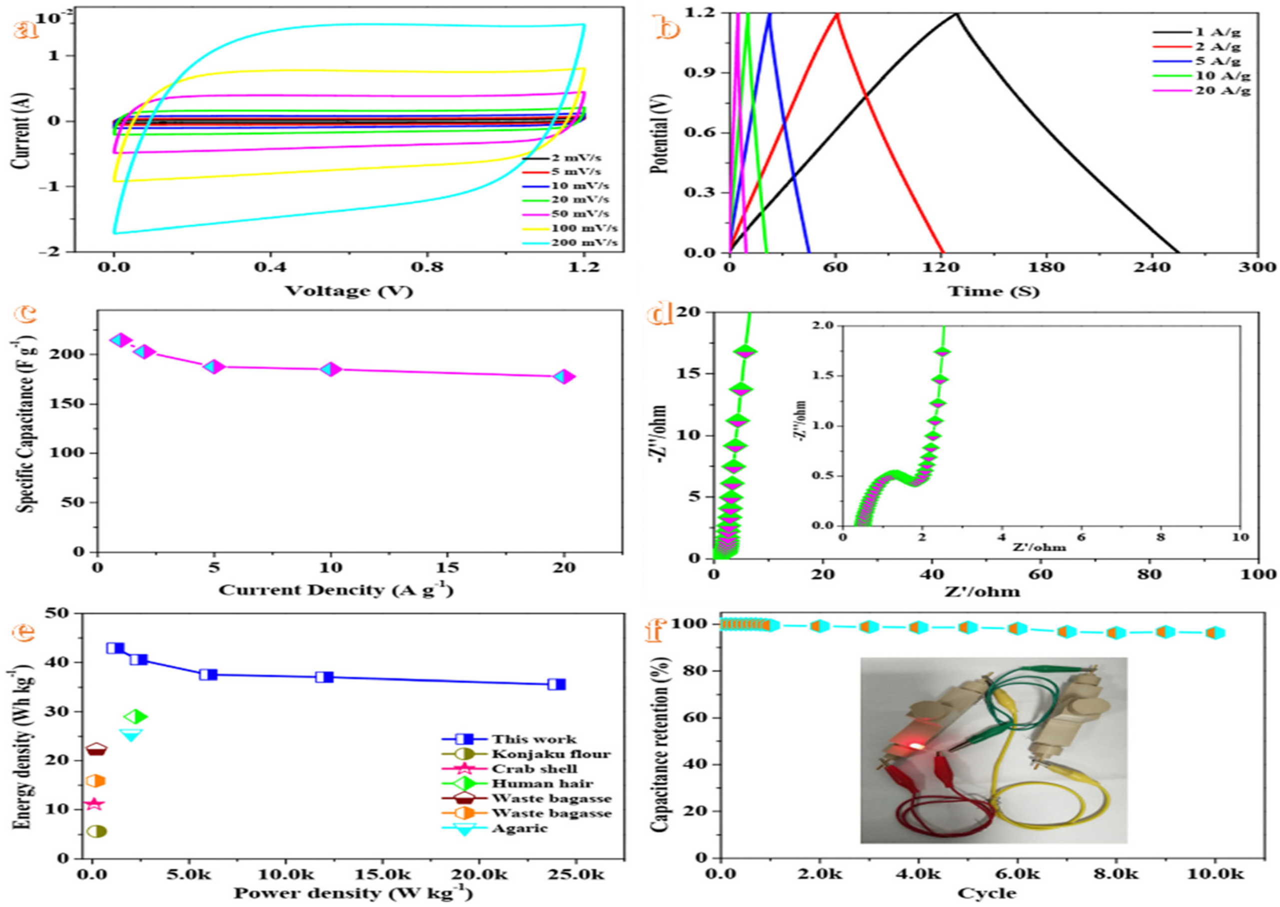

Fig. 4 a) CV curves of the GPAC//GPAC symmetrical supercapacitor at different scan rates in the voltage window range of 0–1.0 V. (b) Galvanostatic charge/discharge curves of the GPAC//GPAC symmetrical supercapacitor at different current densities. (c) Specific capacitances of the as-assembled GPAC symmetrical supercapacitor based on the total mass of the active materials of the two electrodes at different current densities. (d) Nyquist plots of the GPAC//GPAC symmetrical supercapacitor. (e) Ragone plots of the GPAC symmetrical supercapacitor and other previously reported carbon-based symmetric supercapacitors. (f) Cycling performance of the GPAC symmetrical supercapacitor at a current density of 10 A g^{-1} (the inset photograph of lighting LED bulbs).

porous structure, which contributes to accelerating electrolyte diffusion and further improving the electrochemical performance.[69]

The energy density of the supercapacitor (Fig. 4e) reaches a maximum of 42.89 W h kg^{-1} at a power density of 1200 W kg^{-1}. Even at a high power density of 24 k W kg^{-1}, a high energy density of 35.534 W h kg^{-1} is still obtained, which surpass that of many other biomass-based supercapacitors reported in recent years.[52–57] Moreover, the excellent energy/power performances of the device can fill the gap between the high energy density batteries and high power density electrical double-layer capacitors.

To evaluate the long-term cycling stability of the supercapacitor, the device is subjected to 10 000 continuous GCD cycles (Fig. 4f). The device indicates good cycling performances with a capacitance retention rate of 96.27% after 10 000 cycles, which is conducive for practical applications. This result also demonstrates that green pepper-derived carbon materials with a porous structure and defects not only provide additional active sites for electrolyte ions to improve charge storage but also enhance cycling stability.[70] Such a superior performance may be attributed to the stable ionic charge movement and accumulation in the pores.[71] To verify the practical use of the supercapacitor, we have connected the two charged GPAC-4//GPAC-4 supercapacitors connected in series to power a red LED lamp (inset of Fig. 4f), which verifies the practical value of the symmetrical supercapacitor.

Conclusions

To sum up, we have successfully engineered a novel green pepper-derived nanocomposite GPAC-4 by pyrolysis along with a KOH activation strategy. The GPAC-4 electrode for the supercapacitor exhibits excellent rate performance, outstanding cycling stability with a capacitance retention rate of 97.80% after 10 000 cycles, and a high specific capacitance of 863.10 F g^{-1} at 1 A g^{-1}. Moreover, the GPAC-4-based supercapacitor displays a high energy density of 42.89 W h kg^{-1} at a power density of 1200 W kg^{-1}. The excellent electrochemical supercapacitance is mainly ascribed to the synergetic effect of the 3D carbon framework and the doping of heteroatoms, which could provide a great guidance for the synthesis of supercapacitor electrode materials.

Conflicts of interest

There are no conflicts to declare.

Acknowledgements

We gratefully acknowledge financial support from the Faculty of Materials and Energy and Institute for Clean Energy & Advanced Materials, Southwest University and Chongqing Key Laboratory for Advanced Materials and Technologies of Clean Electrical Power Sources and sponsored by the Natural Science Foundation of Chongqing, China (cstc2020jcyj-msxmX0019) and the College Student Innovation and Entrepreneurship Training Program, Southwest University (S202210635259).

References

1 A. Narayanan, A. Siddiqa, N. K. Kodihalli, G. Hegde, D. H. Nagaraju and M. Padaki, *ACS Sustainable Chem. Eng.*, 2023, **11**, 3750.
2 S. Gao, Y. Chen, H. Fan, X. Wei, C. Hu, H. Luo and L. Qu, *J. Mater. Chem. A*, 2014, **2**, 3317.
3 F. Wang, X. Wu, X. Yuan, Z. Liu, Y. Zhang, L. Fu, Y. Zhu, Q. Zhou, Y. Wu and W. Huang, *Chem. Soc. Rev.*, 2017, **46**, 6816.
4 V. S. Bhat, A. Toghan, G. Hegde and R. S. Varma, *J. Energy Storage*, 2022, **52**, 104776.
5 G. A. M. Ali, S. Supriya, K. F. Chong, E. R. Shaaban, H. Algarni, T. Maiyalagan and G. Hegde, *Biomass Convers. Biorefin.*, 2021, **11**, 1311.
6 Z. Zhu and Z. Xu, *Renewable Sustainable Energy Rev.*, 2020, **134**, 110308.
7 C. Shan, H. J. Yen, K. Wu, Q. Lin, M. Zhou, X. Guo, D. Wu, H. Zhang, G. Wu and H. L. Wang, *Nano Energy*, 2017, **40**, 327.
8 L. Sun, X. Wang, Y. Wang and Q. Zhang, *Carbon*, 2017, **122**, 462–474.
9 W. J. Liu, H. Jiang and H. Q. Yu, *Energy Environ. Sci.*, 2019, **12**, 1751.
10 F. Liu, Z. Wang, H. Zhang, L. Jin, X. Chu, B. Gu, H. Huang and W. Yang, *Carbon*, 2019, **149**, 105.
11 M. Athanasiou, S. N. Yannopoulos and T. Ioannides, *Chem. Eng. J.*, 2022, **446**, 137191.
12 B. Liu, M. Yang, D. Yang, H. Chen and H. Li, *J. Power Sources*, 2020, **456**, 227999.
13 M. Liu, K. Zhang, M. Si, H. Yu, L. Chai and Y. Shi, *ChemElectroChem*, 2019, **6**, 3949.
14 P. Simon and Y. Gogotsi, *Nat. Mater.*, 2020, **19**, 1151.
15 C. Y. Chan, Z. Wang, H. Jia, P. F. Ng, L. Chow and B. Fei, *J. Mater. Chem. A*, 2021, **9**, 2043.
16 T. Xu, H. Du, H. Liu, W. Liu, X. Zhang, C. Si, P. Liu and K. Zhang, *Adv. Mater.*, 2021, **33**, 2101368.
17 H. Huang, L. Han, X. Fu, Y. Wang, Z. Yang, L. Pan and M. Xu, *Small*, 2021, **17**, 2006807.
18 D. Zhao, Y. Zhu, W. Cheng, W. Chen, Y. Wu and H. Yu, *Adv. Mater.*, 2020, **33**, 2000619.
19 C. Lei, C. Ji, H. Mi, C. Yang, Q. Zhang, S. He, Z. Bai and J. Qiu, *ACS Appl. Mater. Interfaces*, 2020, **12**, 53164.
20 J. Park, H. H. Rana, J. Y. Lee and H. S. Park, *J. Mater. Chem. A*, 2019, **7**, 16962.
21 S. Saini, P. Chand and A. Joshi, *J. Energy Storage*, 2021, **39**, 102646.
22 S. G. Krishnan, A. Arulraj, M. Khalid, M. V. Reddy and R. Jose, *Renewable Sustainable Energy Rev.*, 2021, **141**, 110798.
23 J. Zhao and A. F. Burke, *J. Energy Chem.*, 2021, **59**, 276.

24 Y. Huang, H. Li, Z. Wang, M. Zhu, Z. Pei, Q. Xue, Y. Huang and C. Zhi, *Nano Energy*, 2016, **22**, 422.

25 J. Qi, Y. Yan, Y. Cai, J. Cao and J. Feng, *Adv. Funct. Mater.*, 2021, **31**, 2006030.

26 K. Zebe, S. Sambasivam, M. Rao and H. J. K. Kummara., *J. Energy Storage*, 2020, **31**, 101.

27 H. Peng, X. Gao, K. Sun, X. Xie, G. Ma, X. Zhou and Z. Lei, *Chem. Eng. J*, 2021, **422**, 130353.

28 N. Yadav, N. Yadav and S. A. Hashmi, *J. Power Sources*, 2020, **451**, 227771.

29 L. Xie, G.-H. Sun, F. Su, X. Guo, Q. Kong, X. Li, X. Huang, L. Wan, W. Song and K. Li, *J. Mater. Chem. A*, 2016, **4**, 1637.

30 Y. Dai, L. Ma, J. Hu, J. Wang, J. Wang, H. Yan, H. Zhang, C. Lai, W. Li and J. C. Zheng, *Electrochim. Acta*, 2021, **371**, 137792.

31 S. Liu, K. V. Sankar, A. Kundu, M. Ma, J. Y. Kwon and S. C. Jun, *ACS Appl. Mater. Interfaces*, 2017, **9**, 21829.

32 Z. Yang, D. Shi, W. Dong and M. Chen, *Chem. – Eur. J.*, 2020, **26**, 1846.

33 R. B. Ambade, S. B. Ambade, R. R. Salunkhe, V. Malgras, S. H. Jin, Y. Yamauchi and S. H. Lee, *J. Mater. Chem. A*, 2016, **4**, 7406.

34 Z. Yang, J. Ma, B. Bai, A. Qiu, D. Losic, D. Shi and M. Chen, *Electrochim. Acta*, 2019, **322**, 134769.

35 L. Sheng, T. Wei, Y. Liang, L. Jiang, L. Qu and Z. Fan, *Small*, 2017, **13**, 17003.

36 B. L. Vijayan, N. K. M. Zain, I. I. Misnon, M. V. Reddy, S. Adams, C. C. Yang, G. M. Anilkumar and R. Jos, *Energy Fuels*, 2020, **34**, 5072.

37 S. Jeon, J. H. Jeong, H. Yoo, H. K. Yu, B. H. Kim and M. H. Kim, *ACS Appl. Nano Mater.*, 2020, **3**, 3847.

38 A. Zhang, L. Yue, D. Jia, L. Cui, D. Wei, W. Huang, R. Liu, Y. Liu, W. Yang and J. Liu, *ACS Appl. Mater. Interfaces*, 2020, **12**, 2591.

39 S. Kumar, G. Saeed, L. Zhua, K. N. Hui, N. H. Kim and J. H. Lee, *Chem. Eng. J*, 2021, **403**, 126352.

40 Q. Xie, S. Zhou, A. Zheng, C. Xie, C. Yin, S. Wu, Y. Zhang and P. Zhao, *Electrochim. Acta*, 2016, **189**, 22.

41 Y. Song, Z. Li, K. Guo and T. Shao, *Nanoscale*, 2016, **34**, 15671.

42 W. Du, X. N. Wang, X. Q. Sun, J. Zhan, H. D. Zhang and X. J. Zhao, *J. Electroanal. Chem.*, 2018, **827**, 213.

43 J. W. Liu, S. X. Min, F. Wang and Z. G. Zhang, *J. Power Sources*, 2020, **466**, 228347.

44 J. L. Goldfarb, G. L. Dou, M. Salari and M. W. Grinstaff, *ACS Sustainable Chem. Eng.*, 2017, **5**, 3046.

45 Y. Yao, C. Ma, J. Wang, W. Qiao, L. Ling and D. Long, *ACS Appl. Mater. Interfaces*, 2015, **7**, 4817.

46 S. Fleischmann, J. B. Mitchell, R. Wang, C. Zhan, D. Jiang, V. Presser and V. Augustyn, *Chem. Rev.*, 2020, **120**, 6738.

47 M. Dilamian, M. Joghataei, Z. Ashrafi, C. Bohr, S. Mathur and H. Maleki, *Appl. Mater. Today*, 2021, **22**, 100964.

48 L. Dou, X. Zhang, H. Shan, X. Cheng, Y. Si, J. Yu and B. Ding, *Adv. Funct. Mater.*, 2020, **30**, 2005928.

49 X. Dong, L. Cao, Y. Si, B. Ding and H. Deng, *Adv. Mater.*, 2020, **32**, 1908269.

50 Y. Li, L. Cao, X. Yin, Y. Si, J. Yu and B. Ding, *Adv. Funct. Mater.*, 2020, **30**, 1910426.

51 S. Jiang, S. Agarwal and A. Greiner, *Angew. Chem., Int. Ed.*, 2017, **56**, 15520.

52 L. F. Chen, Z. H. Huang, H. W. Liang, H. L. Gao and S. H. Yu, *Adv. Funct. Mater.*, 2014, **24**, 5104.

53 J. X. Feng, S. H. Ye, A. L. Wang, X. F. Lu, Y. X. Tong and G. R. Li, *Adv. Funct. Mater.*, 2014, **24**, 7093.

54 R. Guo, L. Zhang, Y. Lu, X. Zhang and D. Yang, *J. Energy Chem.*, 2020, **51**, 342.

55 W. He, Z. Cui, X. Liu, Y. Cui, J. Chai and X. Zhou, *Electrochim. Acta*, 2017, **225**, 151.

56 H. H. Hsu, A. Khosrozadeh, B. Li, G. Luo, M. Xing and W. Zhong, *ACS Sustainable Chem. Eng.*, 2019, **7**, 4766.

57 J. H. Kim, D. Lee, Y. H. Lee, W. Chen and S. Y. Lee, *Adv. Mater.*, 2019, **31**, 1.

58 M. Zhang, D. Yang, S. Zhang, T. Xu, Y. Shi, Y. Liu, W. Chang and Z. Z. Yu, *Carbon*, 2020, **158**, 873.

59 L. Zhu, L. Zong, X. Wu, M. Li, H. Wang, J. You and C. Li, *ACS Nano*, 2018, **12**, 4462.

60 H. Chen, T. Liu, J. Mou, W. Zhang, Z. Jiang, J. Liu, J. Huang and M. Liu, *Nano Energy*, 2019, **63**, 103836.

61 Y. Lei, Q. Wang, S. Peng, S. Ramakrishna, D. Zhang and K. Zhou, *Adv. Energy Mater.*, 2020, **10**, 1902115.

62 B. Ding, S. Huang, K. Pang, Y. Duan and J. Zhang, *ACS Sustainable Chem. Eng.*, 2018, **6**, 177.

63 X. Zhang, J. Zhao, X. He, Q. Li, C. Ao, T. Xia, W. Zhang, C. Lu and Y. Deng, *Carbon*, 2018, **127**, 236.

64 D. C. Wang, H. Y. Yu, D. Qi, M. Ramasamy, J. Yao, F. Tang, K. C. Tam and Q. Ni, *ACS Appl. Mater. Interfaces*, 2019, **11**, 24435.

65 Y. Yang, Y. X. Liu, Y. Li, B. W. Deng, B. Yin and M. B. Yang, *J. Mater. Chem. A*, 2020, **8**, 17257.

66 Z. Zhao, K. Xia, Y. Hou, Q. Zhang, Z. Ye and J. Lu, *Chem. Soc. Rev.*, 2021, **50**, 12702.

67 I. Staffell, D. Scamman, A. Velazquez Abad, P. Balcombe, P. E. Dodds, P. Ekins, N. Shah and K. R. Ward, *Energy Environ. Sci.*, 2019, **12**, 463.

68 Y. Li, Z. Xia, Q. Gong, X. Liu, Y. Yang, C. Chen and C. Qian, *Nanomaterials*, 2020, **10**, 1546.

69 D. Chen, K. Jiang, T. Huang and G. Shen, *Adv. Mater.*, 2020, **32**, 1.

70 A. Noori, M. F. El-Kady, M. S. Rahmanifar, R. B. Kaner and M. F. Mousavi, *Chem. Soc. Rev.*, 2019, **48**, 1272.

71 J. Wang, X. Zhang, Z. Li, Y. Ma and L. Ma, *J. Power Sources*, 2020, **451**, 227794.